Atmospheric Research 214 (2018) 284–295

Contents lists available at ScienceDirect

Atmospheric Research

journal homepage: www.elsevier.com/locate/atmosres

Integration of cloud top heights retrieved from FY-2 meteorological satellite, radiosonde, and ground-based millimeter wavelength cloud radar observations

Yu Wang[a,b], Chunheng Wang[a,*], Cunzhao Shi[a], Baihua Xiao[a]

[a] State Key Laboratory of Management and Control for Complex Systems, Institute of Automation, Chinese Academy of Sciences, University of Chinese Academy of Sciences, Beijing 100190, PR China
[b] School of Software, Shanxi University, Taiyuan 030006, PR China

ARTICLE INFO

Keywords:
Cloud top height
Bayesian decision theory
Data integration
Satellite observation
Radiosonde observation
Radar observation

ABSTRACT

Cloud top height (CTH) is an important parameter monitored in atmospheric observations, which has a significant impact on weather prediction, climate models, and flight services. CTH is typically obtained via three ways, namely, satellite, radiosonde, and ground-based radar, with their corresponding strengths and weaknesses. Traditionally, many studies have focused on independent comparison and analysis of CTHs retrieved from different observations. The researches on how to improve the reliability of the CTH by integrating multiple cloud measurements are rare in the literature despite the significance of this strategy to practical meteorological forecast and disaster prevention improvement. An integration technique of different CTHs retrieved from Fengyun 2 (FY-2) meteorological satellite, radiosonde, and ground-based millimeter wavelength cloud radar observations by using Bayesian decision theory is proposed in this study. A dataset is collected in Beijing, China for 12 months from June 2015 to May 2016 to validate the integration effect. Experimental results show that the integration observations improve the accuracy of single observations. Integration observations are more closely correlated with "true" CTH observations than the single observations. These all show the effectiveness of the proposed multiple source data integration strategy.

1. Introduction

Cloud height is an important parameter that is monitored by the World Meteorological Organization (WMO), given the significant impact of this parameter on surface radiation budget and cloud microphysical property retrieval (Viúdez-Mora et al., 2015; Hirsch et al., 2011; Martucci and O'Dowd, 2011; Garrett and Zhao, 2013). The vertical structure of clouds described by cloud base height (CBH) and cloud top height (CTH) plays a key role on weather prediction, climate models, and flight services. This study focuses on CTH, not only for its impact on radiation, numerical weather prediction, and the detection of cosmic rays, but also for its link to rain production (Naud et al., 2003; Merino et al., 2016; Genkova et al., 2007; Wang et al., 2018a). An accurate and timely access to information on cloud parameters, such as the CTH, is necessary, but these data remain uncertain considering the complexity of changes in temporal and spatial scales (Wang et al., 2018a; Stephens, 2005).

Clouds are generally observed via three ways, namely, space-based satellite, air-based radiosonde, and ground-based remote sensing. Correspondingly, the CTHs retrieved from these observations are different given the various observation systems, instrument performances, and retrieval methods. Each method has its own strengths and weaknesses. An accurate satellite observation with different spatial and temporal resolutions is widely utilized in large-scale surveys of mid- and high-level clouds and CTH retrieval. However, Dev et al., (2016, 2017) and Wang et al., (2018b) indicated that, satellite observations cannot provide sufficient temporal and spatial resolutions for localized and short-term cloud analyses, such as local weather prediction, over a particular area. In this case, small clouds may be easily overlooked, and low or thin clouds are easily confused because of their similar brightness and temperature (Heinle et al., 2010; Ricciardelli et al., 2008; Dybbroe et al., 2005). In addition, their retrieval capability is limited considering the complexity of the underlying surface. Thus, the CTH retrieved from satellite may not be sufficiently accurate.

Air-based radiosonde remote sensing observation is advantageous in detecting clouds, but this method is considerably costly. Moreover, the

* Corresponding author.
E-mail addresses: wangyu@sxu.edu.cn, chunheng.wang@ia.ac.cn (C. Wang).

https://doi.org/10.1016/j.atmosres.2018.07.025
Received 14 May 2018; Received in revised form 10 July 2018; Accepted 31 July 2018
Available online 10 August 2018
0169-8095/

detection can only be performed twice a day and noise easily affects the observation. Ground-based remote sensing equipments, such as millimeter wavelength cloud radar and laser ceilometer, acquire cloud information by launching the millimeter-wave or laser from the ground surface. Ground-based observation is available at a low cost and a high resolution and provides accurate local cloud information. However, as pointed out by Wang et al., (2018a), this observation is only local, and the spatial coverage is limited by a density distribution of the observation stations. Long-wavelength radars are less sensitive to small cloud particles; moreover, lidar signals can be attenuated before reaching the top of moderately thick clouds, and ceilometers do not typically penetrate the lowest cloud layer to measure the boundaries of upper-level cloud layers (Wang et al., 1999). Therefore, cloud observation by integrating multiple cloud measurements will significantly correct the results of the CTHs retrieved from different observations and improve the reliability of the CTH retrieval (Lv et al., 2003; Oh et al., 2016).

Several studies have compared and verified the CTH data derived from multiple cloud measurements. For example, in early studies, Wang et al., (1999) applied a combination of radiosonde, 8 mm cloud radar, laser cloud gage, and geostationary meteorological satellite data to observe the changes in the vertical structure of clouds and analyzed the difference between the four observations. Hollars et al., (2004) evaluated the accuracy and limitations of both ARM 35 GHz Millimeter Wave Cloud Radar (MMCR) and GMS-5 satellite retrievals by comparing the CTHs from each instrument. Weisz et al., (2007) compared four CTH retrievals from Atmospheric Infrared Sounder (AIRS), Moderate Resolution Imaging Spectroradiometer (MODIS), CloudSat, and Cloud-Aerosol Lidar and Infrared Pathfinder Satellite Observation (CALIPSO) and discussed the strengths/shortcomings of different CTH products. Marchand et al., (2010) showed that the differences in the joint histograms of CTHs from Multiangle Imaging Spectro-Radiometer (MISR), International Satellite Cloud Climatology Project (ISCCP), and MODIS are notable by comparing annually averaged joint histograms on global and regional scales.

Recently, Zhang et al., (2014) compared the CTHs retrieved by the IASI detector on METOP-A satellites in Europe and W-band (95 GHz) ground-based cloud radar (WACR) observation. The results showed that the IASI CTH was lower than that obtained from the WACR observation. Oh et al., (2016) studied the verification and correction of CBH and CTH retrievals from Ka-band cloud radar in Boseong, Korea by using a ceilometer (CL51) and the Communication, Ocean, and Meteorological Satellite (COMS) observations. Wang et al., (2018a) compared and analyzed CTHs derived from Fengyun 2 (FY-2) meteorological satellite and ground-based millimeter wavelength cloud radar for the time period from June 2015 to May 2016 over China.

However, most of these studies have focused on independent comparison and analysis of the CTHs retrieved from different observations, but have not considered the integration and synergy of multiple cloud measurements to improve the reliability of the CTH retrieval. Thus, this study uses Bayesian decision theory to integrate different CTHs retrieved from FY-2 meteorological satellite, radiosonde, and ground-based millimeter wavelength cloud radar observations. The proposed space-air-ground integrated cloud observation will deliver accurate cloud information by integrating the strength of multiple observations. The proposed strategy can further improve the capacity of meteorological forecast and disaster prevention.

Cloud top temperature (CTT) data from the FY-2 satellite, radiosonde, and cloud radar reflectivity data are collected to retrieve the CTHs from June 2015 to May 2016. First, the CTH integration results from the three observations validate the effectiveness of the proposed integration technique. Second, the accuracy is better in the integrated CTH than in the single observations.

The remainder of this study is organized as follows. Section 2 briefly reviews the FY-2 satellite, radiosonde, and cloud radar data and the CTH retrievals, and Section 3 describes the proposed integration strategy and algorithm based on Bayesian theory. Section 4 presents the experimental results as well as the details of the experiments. Section 5 gives the conclusions of this study.

2. Data and preprocessing

The data used in this analysis correspond to a time interval spanning 12 months from June 2015 to May 2016 in Beijing, China.

2.1. FY-2 satellite observation and the CTT retrieved CTH

The FY-2 satellite is a geosynchronous orbiting meteorological satellite developed by China. This satellite is used to collect meteorological, climatological, hydrological, and oceanographic data. This study used data from the FY-2F satellite. However, the FY-2G product replaced unavailable FY-2F data. The stationary satellite orbits the earth in the equatorial plane at a height of 35,785 km above the equator and a longitude of 112°E. The Stretched Visible and Infrared Spin Scan Radiometer (S-VISSR) on FY-2F satellite monitors the weather conditions in 5 channels: 4 infrared channels and 1 visible channel. The wavelength of visible channel with 1.25 km resolution ranges from 0.55 μm to 0.75 μm, and the wavelengths of four infrared channels with 5 km resolution are between 10.3 μm and 11.3 μm, 11.5 μm and 12.5 μm, 6.3 μm and 7.6 μm, and 3.4 μm and 4.0 μm, respectively.

Cloud properties, such as the CTH, are indirectly derived from the FY-2 satellite data. However, satellite CTH can be retrieved by using an FY-2 CTT product, which uses a single-channel infrared window area retrieval (Oh et al., 2016). A database of CTT look-up tables was established by considering the radiation effects of an 11 μm window area and the influence of surface temperature and optical thickness (Wang et al., 2018a). Specifically, the FY-2 satellite CTH was calculated by associating the CTT with cloud height using an atmospheric temperature profile and then searching for the CTT value in the corresponding atmospheric profile data to find a temperature that matches the height.

The CTT values observed from FY-2F satellites with one year from June 1, 2015 to May 31, 2016 were obtained from the Fengyun Satellite Data Center of China. The time resolutions of the observation are 0.5 h and 1 h in the time intervals of June 1, 2015 – November 30, 2015 and December 1, 2015 – May 31, 2016, respectively.

2.2. Cloud radar observation and the CTH determination

The original data were observed by the Ka-band Doppler cloud radar system at Beijing Nanjiao Weather Observatory (39°48′22″*N*, 116°28′10″*E*, 32 m above sea level). This radar system uses a pulse compression technology to solve the distance resolution problem and consider short-range blind spots. The vertical and temporal resolutions of radar are 30 m and 1 min, respectively. Cloud location or cloud height was determined by measuring the distance of echo signals returned by the radar beam when detecting the liquid water or ice crystals in the cloud. The echo signals correspond to cloud locations in the ideal situation.

However, determining cloud boundary may be easily disturbed by random noise or continuous non-cloud clutter at 1 km in practice. Thus, noise should be filtered out by using the Gaussian filtering method. The second step determined the cloud boundary on the basis of reflectivity

threshold. The third step was a quality control stage that improved the accuracy of cloud boundary determination. For details, readers may refer to Wang et al., (2018a).

Corresponding to the data acquisition time period of FY-2 satellite, the cloud radar observational data from 0:00 on June 1, 2015 to 24:00 on May 31, 2016 (Beijing time) over a time span of 1 year were obtained.

2.3. L-band radiosonde observation and the CTH retrieval

A radiosonde is a telemetry instrument carried into the atmosphere typically by a weather balloon with a radiosonde and a radio theodolite or a wind measuring radar that measures various atmospheric parameters and transmits signals by radio to a ground receiver. An L-band radiosonde system located in Beijing Nanjiao meteorological observation station is composed of GFE(L)1 L-band secondary windfinding radar and GTS1 digital radiosonde. This system continuously and automatically observes atmospheric meteorological factors, such as temperature and relative humidity, and the observation range and accuracy of temperature are from −80 °C (Celsius) to 40 °C and 0.2 °C. Furthermore, the accuracies of humidity are 0.05 and 0.10 for the above and below −25 °C cases, respectively. The sampling period is 1.2 s, and the sampling frequency is 50 Hz.

The WR95 method proposed by Wang and Rossow, (1995) is the most commonly used method to determine the cloud layers by using the threshold value of relative humidity and the plus or minus changes in the relative humidity of the CTH and CBH. In particular, Zhang et al., (2010) proposed an improved version of WR95 method by setting the minimum of relative humidity and removing the determination of the changes of relative humidity, which is referred as the ZHA10 method. Wang et al., (2018a); Costa-Surós et al., (2014) further validated the superiority of ZHA10 method by comparing several techniques based on radiosonde profiles and ground-based remote sensing measurements. Thus, this method is adopted in this study.

This study used the measured L-band sounding data with a balloon placed 158 m west of the cloud radar station. The vertical resolution of the profile was approximately 8 m. This high vertical resolution facilitated an accurate search and calculation of the cloud height but had a low temporal resolution because the radiosonde observation was recorded twice a day, that is, 07:15 and 19:15 (Beijing time). The available humidity data cover the time period of June 1, 2015 and May 31, 2016.

3. Integration technique based on Bayesian theory

Data integration or data assimilation is a process in which observational data are fused with scientific information (Wikle and Berliner, 2007). It is a mathematical discipline that seeks to optimally combine theory in the form of a numerical model with observations. There may be a number of different goals sought, for example, to determine the optimal state estimate of a system, to determine initial conditions for a numerical forecast model, to interpolate sparse observation data using knowledge of the system being observed, and to train numerical model parameters based on observed data. Several monographs and review papers have described various methods and approaches to data integration (Talagrand, 1997; Kalnay, 2003; Bennett, 2002). In this study, we explore the topic from a Bayesian perspective. The Bayesian paradigm provides a coherent probabilistic approach for combining information and thus is an appropriate framework for data integration.

3.1. Bayesian inference

Bayesian inference is a fundamental theory in machine learning community (Wikle and Berliner, 2007; Hastie et al., 2009.) Wikle and Berliner, (2007) highlighted that Bayesian inference consists of three processes. First, a full probability model is used to formulate the joint probability distribution of all observed and unobserved data components. Second, the conditional probability distribution of the unobserved quantities of interest is found on the basis of the observed data. Finally, the performance of the fitted model is evaluated.

Specifically, if denoting X be the unobserved quantities of interest and Y be the data, the full probability model can always be factored into components:

$$p(x,y) = p(y \mid x)p(x) = p(x \mid y)p(y) \tag{1}$$

Applying Bayes' Theorem (Bayes' Rule), we have

$$p(x \mid y) = \frac{p(y \mid x)p(x)}{p(y)} \tag{2}$$

where $p(y|x)$ refers to the data (conditional) distribution, which is used to describe the available process of observation data y given the unobserved quantity x. For example, in this study, X represents the true (unobserved) CTH, and Y represents the observations of CTH, then $p(y|x)$ quantifies the distribution of measurement errors in observing CTH. $p(x)$ refers to the prior distribution, which quantifies a priori understanding of the unobserved quantities of interest. If X denotes the CTH, the prior distribution may be estimated based on the historical information. $p(y)$ refers to the marginal distribution with the form of $p(y) = \int p(y|x)p(x)dx$. It represents the probability of observation y whatever the x is, and it is always thought of as a constant. This distribution $p(x|y)$ of the unobserved components given the data is our primary focus for inference, which is denoted as posterior distribution. Posterior distribution can be considered an update of prior knowledge on X as summarized in $p(x)$ given the actual observations y. For example, the distribution represents the probability of the true CTH value being x when the observed CTH is y.

In this study, the goal of multiple source data integration from satellite, radiosonde, and ground-based cloud radar is to provide a credible CTH observation. Moreover, Bayesian theory provides a distribution description of the true CTH by combining prior and observation information. Thus, Bayesian theory is appropriately used to integrate the CTHs retrieved from satellite, radiosonde, and ground-based cloud radar. The theory essentially explores the data assimilation problem from a coherent probability distribution perspective.

3.2. Bayesian integration framework

Bayesian integration technique is a commonly used data assimilation technique developed by Bayesian theory. For inferring the posterior distribution $p(x|y)$, the prior distribution $p(x)$ and data distribution $p(y|x)$ should be determined beforehand. Normal distribution is a natural choice. Assume we have the prior distribution that X follows a Normal distribution of $N(\mu, \tau^2)$ with mean μ and variance τ^2. Conditioned on the true value of $X = x$, assume we have n independent observations $Y = (Y_1, \ldots, Y_n)$ and it follows $N(x, \sigma^2)$, i.e., $Y_i|x \sim N(x, \sigma^2)$. Then,

$$p(y \mid x) = \prod_{i=1}^{n} \frac{1}{\sqrt{2\pi\sigma^2}} \exp\{-(y_i - x)^2/(2\sigma^2)\} \tag{3}$$

$$\propto \exp\left\{-\sum_{i=1}^{n}(y_i - x)^2/(2\sigma^2)\right\} \tag{4}$$

By using Bayes' rule, we have

$$\begin{aligned} p(x \mid y) &\propto \exp\left\{-\left[\sum_{i=1}^{n}(y_i - x)^2/(2\sigma^2) + (x-\mu)^2/(2\tau^2)\right]\right\} \\ &\propto \exp\{-(x-\mu_1)^2/(2(\sigma_0^{-2}+\tau^{-2})^{-1})\} \end{aligned} \tag{5}$$

where

$$\mu_1 = (\overline{y}\sigma_0^{-2} + \mu\tau^{-2})/(\sigma_0^{-2}+\tau^{-2}),\quad \sigma_0^2 = \sigma^2/n,\quad \overline{y} = \sum_{i=1}^{n} y_i/n$$

That is, the posterior distribution $p(x|y)$ is also a Normal distribution with mean μ_1 and variance $(\sigma_0{}^{-2} + \tau^{-2})^{-1}$, i.e.,

$$X|y \sim N((\overline{y}\sigma_0^{-2} + \mu\tau^{-2})/(\sigma_0^{-2}+\tau^{-2}), (\sigma_0^{-2}+\tau^{-2})^{-1}). \tag{6}$$

Furthermore, the posterior mean and variance can be rewritten as

$$\begin{aligned} E(X \mid y) &= (\overline{y}\sigma_0^{-2} + \mu\tau^{-2})/(\sigma_0^{-2}+\tau^{-2}) = \omega_y\overline{y} + \omega_\mu\mu \\ &= \mu + K(\overline{y} - \mu) \end{aligned} \tag{7}$$

$$Var(X \mid y) = (\sigma_0^{-2}+\tau^{-2})^{-1}) = (1-K)\tau^2 \tag{8}$$

where $\omega_y = \tau^2/(\sigma_0{}^2 + \tau^2)$, $\omega_\mu = \sigma_0{}^2/(\sigma_0{}^2+\tau^2)$, $K = \tau^2/(\sigma_0{}^2+\tau^2)$.

Based on above Bayesian integration theory under Normal assumption, the CTH integration equation can be written as

$$X^1 = X^0 + K(Y - X^0) \tag{9}$$

where X^0 is the initial CTH, Y is the CTH observation information, and X^1 is the integrated CTH. Thus, the space-air-ground CTH integration can be described as the following process.

Remark 1: Actually, Eqs. (7) and (8) provide a good explanation of how "Bayesian integration" is performed. The prior mean μ is adjusted toward the sample estimate $\overline{y}$ by a "gain" of K, and the posterior variance is updated from the prior variance by a coefficient of $1 - K$.

In addition to the above integration algorithm based on using two time Bayes' rule, another integration approach is available. The space-air-ground CTH integration is performed by simultaneously introducing the L-band radiosonde and satellite information into the initial cloud radar observation.

Specifically, assume we are interested in a process X that has prior distribution, $X \sim N(\mu, \tau^2)$. We observe the 2×1 data vector Y and assume the following data model, $Y|x \sim N(hx, R)$, where the 2×1 vector h and the 2×2 observation covariance matrix R are to be known. Similarly, we can show that the posterior distribution of $X|y$ is also a normal distribution, i.e.,

$$\begin{aligned} X|y \ \sim & N((h^TR^{-1}h + \tau^{-2})^{-1}(h^TR^{-1}y + \tau^{-2}\mu), \\ & (h^TR^{-1}h + \tau^{-2})^{-1}). \end{aligned} \tag{10}$$

The posterior mean and variance can be rewritten as

$$E(X \mid y) = \mu + k^T(y - h\mu), \tag{11}$$

$$Var(X \mid y) = (1 - k^Th)\tau^2, \tag{12}$$

where $k = \tau^2(R + \tau^2 hh^T)^{-1}h$.

Similar to Eq. (9), the integration equation can be written as

$$X^1 = X^0 + k^T(Y - hX^0), \tag{13}$$

The corresponding integration process can be described as the following Algorithm 2.

Remark 2: In view of the independence of the cloud radar, radiosonde, and satellite observations, the coefficient $h = (1, 1)^T$, and the matrix R is equal to:

$$R = \begin{pmatrix} \sigma_1^2 & 0 \\ 0 & \sigma_2^2 \end{pmatrix}. \tag{14}$$

Algorithm 1 Space-air-ground CTH integration

1. Treat the cloud radar observation as the prior CTH X^0
2. Treat the distribution of L-band radiosonde observation Y as the data distribution
3. Compute the weight K and the integrated CTH observation X^1 based on Eq. (9)
4. Treat the integrated observation as the new initial CTH X^0_{new}
5. Treat the satellite observation as the new data observation Y_{new}
6. Compute the new weight K_{new} and the new integrated CTH observation X^1_{new} based on Eq. (9)

Remark 3: Typically, in this integration framework, μ, τ^2, σ^2, ${\sigma_1}^2$, and ${\sigma_2}^2$ are all unknown parameters. In practical computation, these parameters are estimated by statistical method. The sample mean and sample variance are the commonly used methods.

Algorithm 2 Space-air-ground CTH integration

1. Treat the cloud radar observation as the prior CTH X^0
2. Treat the L-band radiosonde and satellite observations as the two-dimensional data information
3. Compute the weight K, the coefficient h, and the integrated CTH observation X^1 based on Eq. (13)

4. Experimental analysis and comparison

For comparing the CTHs from the cloud radar, radiosonde, and satellite observations, the samples in a time interval spanning 12 months from June 2015 to May 2016 over China are selected. The time-matched cloud radar and radiosonde data are collected in Beijing Nanjiao Weather Observatory. The data of the corresponding time of passing territory from the FY-2 satellite of China are also collected. Spatial matching is based on the location of latitude and longitude information of the radar station to extract the corresponding locations of the satellite observations from the CTT products. A total of 218 effective data points were obtained from the satellite, radar, and radiosonde records by removing missing and inconsistent observations.

4.1. Comparison of three CTH observations

In this subsection, we provide different comparisons of the CTH data derived from satellite, radar, and radiosonde observations for all time points and different monthly time intervals. Experimental results show the feasibility and necessity of integrating the satellite, radar, and radiosonde CTH observations.

Fig. 1 illustrates the time series plots of CTH series for the satellite, radiosonde, and radar observations. In this figure, the three CTH series from different observations have a similar changing trend. Hence, a close relationship is observed among the satellite, radiosonde, and radar observations. The correlations of these observations further validate this point. For example, the correlation of the satellite and radar observations computed by all samples even achieves 0.65. These results implied that the satellite, radar, and radiosonde CTH observations can be feasibly and effectively integrated. However, the differences of the three observations are easily observed. The average CTH changes from 5.91 km of satellite observation to 6.03 and 7.23 km of radiosonde and radar observations. The change in variance is from 3.46 of radiosonde to 6.65 and 6.93 of satellite and radar, respectively.

Table 1 summarizes the monthly average observation results of three CTHs from June 2015 to May 2016. The change trends of the three observations are similar, although the radar observation exhibits the maximal CTH values for all months. The data from Jun 2015, Jul 2015, Aug 2015, Sep 2015, Oct 2015, Apr 2016, and May 2016 indicate large CTH values, whereas other months (Nov 2015, Dec 2015, Jan 2016, Feb 2016, and Mar 2016) have small CTHs. However, the difference in the CTHs from various observations is obvious. The maximal and minimal differences among these CTHs are 2.53 and 0.49 km, respectively. Thus, integrating different observations and providing accurate CTH require corresponding solutions.

4.2. Integration of three CTH observations

The theoretical analysis in Section 3 reveals that a basic assumption of this integration frame is that the data follows a Normal distribution. Thus, the normality of the three CTH observations should be first examined. Fig. 2 depicts the results of the Q-Q plots for the Normal test.

The CTHs from the different observations nearly follow the Normal distributions, although fluctuations are observed as demonstrated in Fig. 2(a), (b), and (c). That is, the proposed integration frame is appropriate for the CTH integration from the satellite, radar, and radiosonde observations. The integration results are presented in Table 2.

In the CTH values listed in Table 2, the two integrated CTHs are the compromise results of the satellite, radar, and radiosonde values. In fact, the result is as expected. This conclusion is easily theoretically inferred from the Eqs. (9) and (13). The change in variance is obvious in the integration operation. The integrated CTH observations are stable, and the variances of the integrated CTHs are half of that of the satellite and radar CTHs. However, these comparisons are insufficient for validating the superiority of the proposed integrated technique. Thus, three performance measure indexes are adopted to test the integration performance in the next subsection.

4.3. Performance comparison

The evaluation of the integration results is performed by examining the integrated accuracy of the proposed integration strategy from the perspective of statistical analysis. Owing to the accurate local detection and high time resolution of radar observation, the radar retrieved CTH of a two-hour delay is adopted as the “true” value to compare the

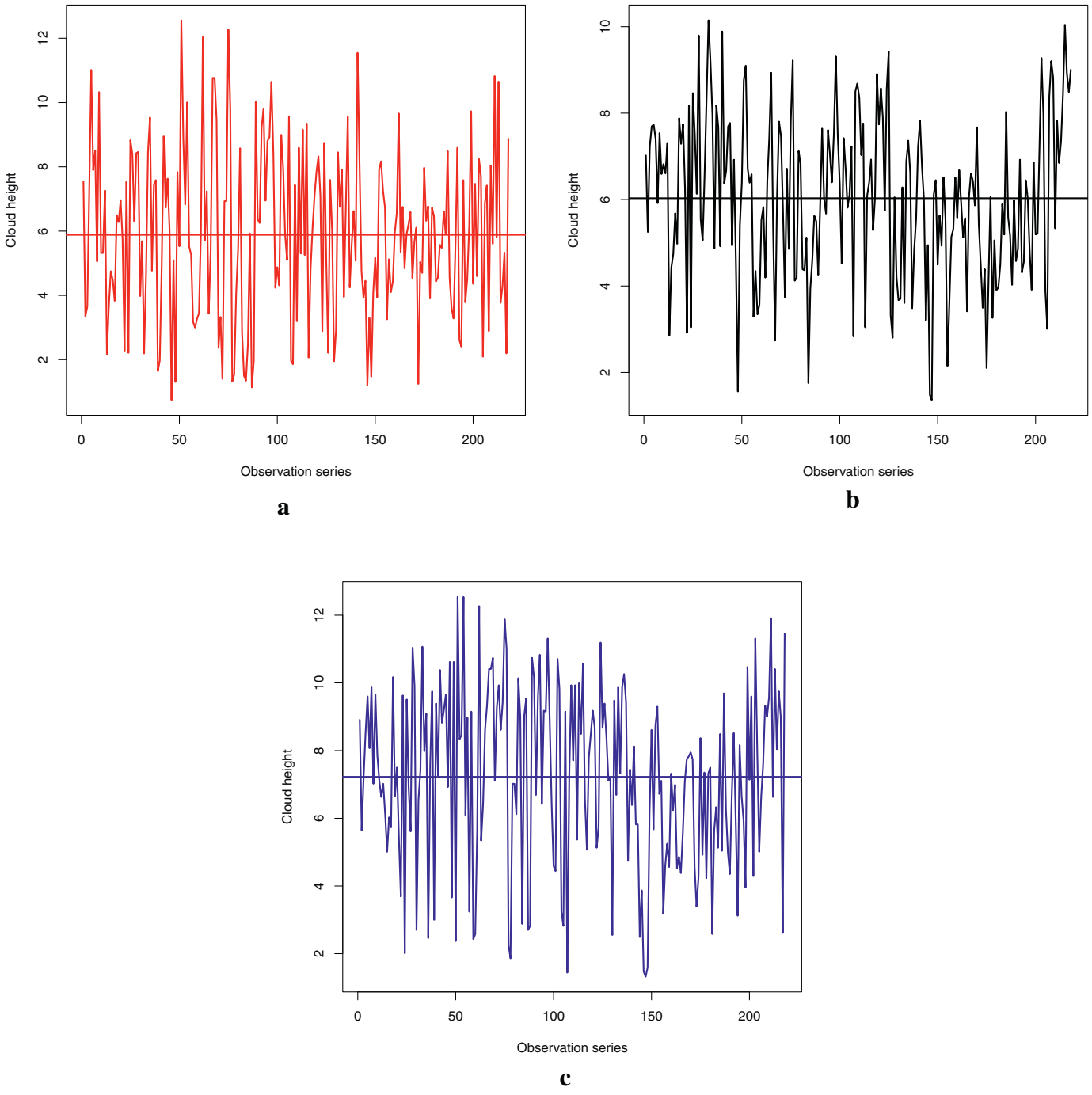

Fig. 1. Time series plots of CTH series for (a) satellite, (b) radiosonde, and (c) radar observations.

integrated results. Generally, the change in the CTH value in 2 h is relatively small. The current satellite, radar, and radiosonde CTH observations are respectively interpolated to that after 2 h by modeling linear modelization. The satellite, radar, and radiosonde CTH values obtained by the linear prediction are compared with the "true" CTH values.

Three performance measure indexes are introduced to compare the before and after performances of integrating the CTH observations. The index of bias (error) is the difference between the observed and "true" values. A minimal bias will make the result accurate. The mean square error (MSE) measure is the most commonly used performance measure index for evaluating the experimental results by

Table 1
Average CTH observations with different months (unit: km).

Period	Satellite CTH	Radiosonde CTH	Radar CTH
Jun 2015	6.11	6.67	7.26
Jul 2015	5.91	6.29	8.09
Aug 2015	5.68	5.60	7.71
Sep 2015	6.54	6.85	7.54
Oct 2015	5.77	5.59	8.12
Nov 2015	5.54	5.16	5.65
Dec 2015	5.23	4.98	6.48
Jan 2016	5.59	4.42	5.65
Feb 2016	5.45	5.48	6.33
Mar 2016	4.91	5.50	6.39
Apr 2016	6.46	6.09	7.40
May 2016	6.21	8.20	8.88

combining the bias and variance. Another measure is the correlation coefficient, which is used to analyze the degree of linear correlation between two variables. Formally, the three indexes can be expressed in the following forms:

$$Bias = \frac{1}{n}\sum_{i=1}^{n}(CTH_i^O - CTH_i^T) \tag{15}$$

$$MSE = \frac{1}{n}\sum_{i=1}^{n}(CTH_i^O - CTH_i^T)^2 \tag{16}$$

$$Corr = \frac{Cov(CTH^O, CTH^T)}{\sqrt{Var(CTH^O)Var(CTH^T)}} \tag{17}$$

where CTH^O and CTH^T refer to the interpolated and "true" satellite (or radiosonde, or radar) CTH observation vectors, respectively, Cov () and $V\,ar$() refer to the covariance and variance functions, and n is the sample size.

The data should be divided into two, training and test, subsets to model the relation of the CTH observations in the two-hour time interval. The training set is used to fit the linear model, whereas the test set is used to provide the prediction value. In practice, a K-fold cross validation with a number of times training and validation is constantly applied to effectively evaluate the performance of different methods. In this experiment, we set $K = 5$.

Formally, the data set D is split into K disjoint and equal-sized blocks, denoted as T_k, $k = 1, 2, \ldots, K$. Let D_k be the training set obtained by removing the elements in T_k from D. This procedure is repeated K times, such that each element in the training data set repeated same times for training and testing. Then, the fitted linear model can be written as

$$\widehat{CTH}_{T_k} = a^*_{D_k} \cdot CTH_{T_k} + b^*_{D_k} \tag{18}$$

where coefficients of $a_{D_k}{}^*$ and $b_{D_k}{}^*$ are computed by the training set D_k, CTH_{T_k} represents the sample in the test set T_k, and $\widehat{CTH}_{T_k}$ refers to the prediction value. The fitted linear models for the proposed two integration techniques are displayed in Figs. 3 and 4, correspondingly. The scatter plots of the interpolated and "true" CTHs in Figs. 3 and 4 do not present any specific change trend. The data imply that the interpolation based on the linear model may be appropriate. A new delayed two-hour CTH prediction of the current CTH observation is presented for the performance comparison of different observations by modeling linear modelization. The comparison results are summarized in Table 3.

Table 3 shows that the integration observations with integration algorithms 1 and 2 exhibit the superior performance to the single CTH observation of satellite, radiosonde, and radar whether for the correlation coefficient measure or for the mean square error and bias measures. The MSE and bias are lower in the integration observations than in the single observations. The correlation coefficient is larger in the integration observations than in the single observations. The radiosonde observation is poorest, and the satellite and radar observations are similar for the three measures. For example, the MSEs are 5.95, 5.14, 5.11, 4.87, and 4.99 for radiosonde, satellite, radar, integration 1, and integration 2 observations, respectively. However, the MSE of the integration 1 observation is reduced about 4.7%, 5.3%, and 18.2% compared with the radar, satellite, and radiosonde observations, as displayed in Table 3.

Furthermore, we provide the comparison results for the different seasons (spring, summer, autumn, and winter), where spring refers to Mar, Apr, and May 2016, summer refers to Jun, Jul, and Aug, 2015, autumn refers to Sep, Oct, and Nov, 2015, and winter refers to Dec, 2015, Jan, and Feb, 2016. Fig. 5 plots the small change in the MSE for the radiosonde observation. However, other observations (satellite, radar, and integration observations) exhibit a large MSE change. The MSEs of the integration observations are the smallest among all observations for spring, summer, and autumn. For winter, the MSE of the radiosonde observation is the smallest and the MSEs of the integration observations are superior to the satellite and radar observations.

For the correlation coefficient measure, a similar change in the MSE measure is observed, as shown in Fig. 6. The correlation coefficients of the integration and "true" observations are the largest for spring, summer, and autumn. For winter, the correlation coefficients of the radiosonde and "true" observations are the largest, and the correlation coefficients are larger in the integration and "true" observations than in the satellite and radar observations.

The performances are poorer in the radiosonde observation than in the other observations for spring, summer, and autumn. However, two measure indexes indicated a superior performance for winter. The correlation coefficients of the satellite and radar observations and the "true" observation present negative values. This result may be due to the small number of the collected CTH samples because only 15 samples are obtained in the three winter months of Dec, 2015, Jan, and Feb, 2016. Further analysis is underway.

5. Conclusions

In this study, two integration algorithms of different CTHs retrieved from FY-2 meteorological satellite, radiosonde, and ground-based millimeter wavelength cloud radar observations based on Bayesian decision theory are proposed to improve the reliability of the CTH observation. A dataset collected from China in a time interval spanning 12 months from June 2015 to May 2016 is used to validate the feasibility and effectiveness of the proposed integration algorithms. First, the comparison of different CTH observations in the collected dataset shows the necessary of integration. Second, the Normal test of the CTH series shows the feasibility of the Bayesian integration frame. Finally, experimental analysis shows that the integration observations improve the accuracy of the single observations, which have more closely correlation with the "true" CTH observation than that of the single observations. These all show the effectiveness of the proposed multiple source data integration strategy.

However, this study is only focused on analyzing the integration

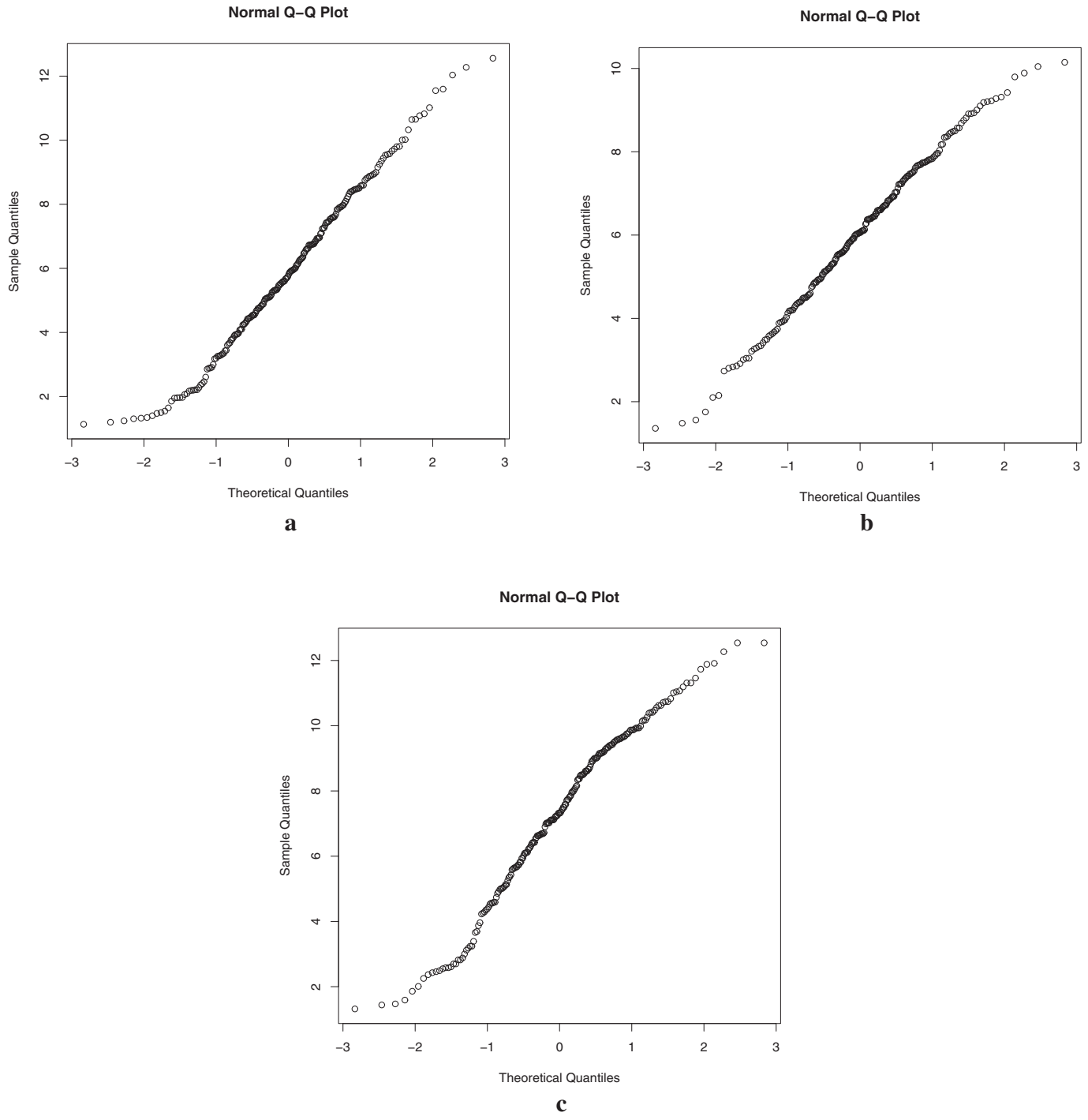

Fig. 2. Q-Q plots for (a) satellite, (b) radiosonde, and (c) radar observations.

Table 2
Integrated CTH observations.

	Average CTH values	Variance
Satellite	5.91	6.65
Radiosonde	6.03	3.46
Radar	7.23	6.93
Integration algorithm 1	6.26	3.36
Integration algorithm 2	6.37	3.27

of CTHs obtained from different observations on a single observation site. In future works, we will direct the study on spatial and temporal integrated integration strategy based on multiple source CTH data, and on acquiring the spatial and temporal distribution map of CTH with high accuracy. Furthermore, we will also discuss the integration strategy for multiple type data with CTH, CBH and cloud thickness.

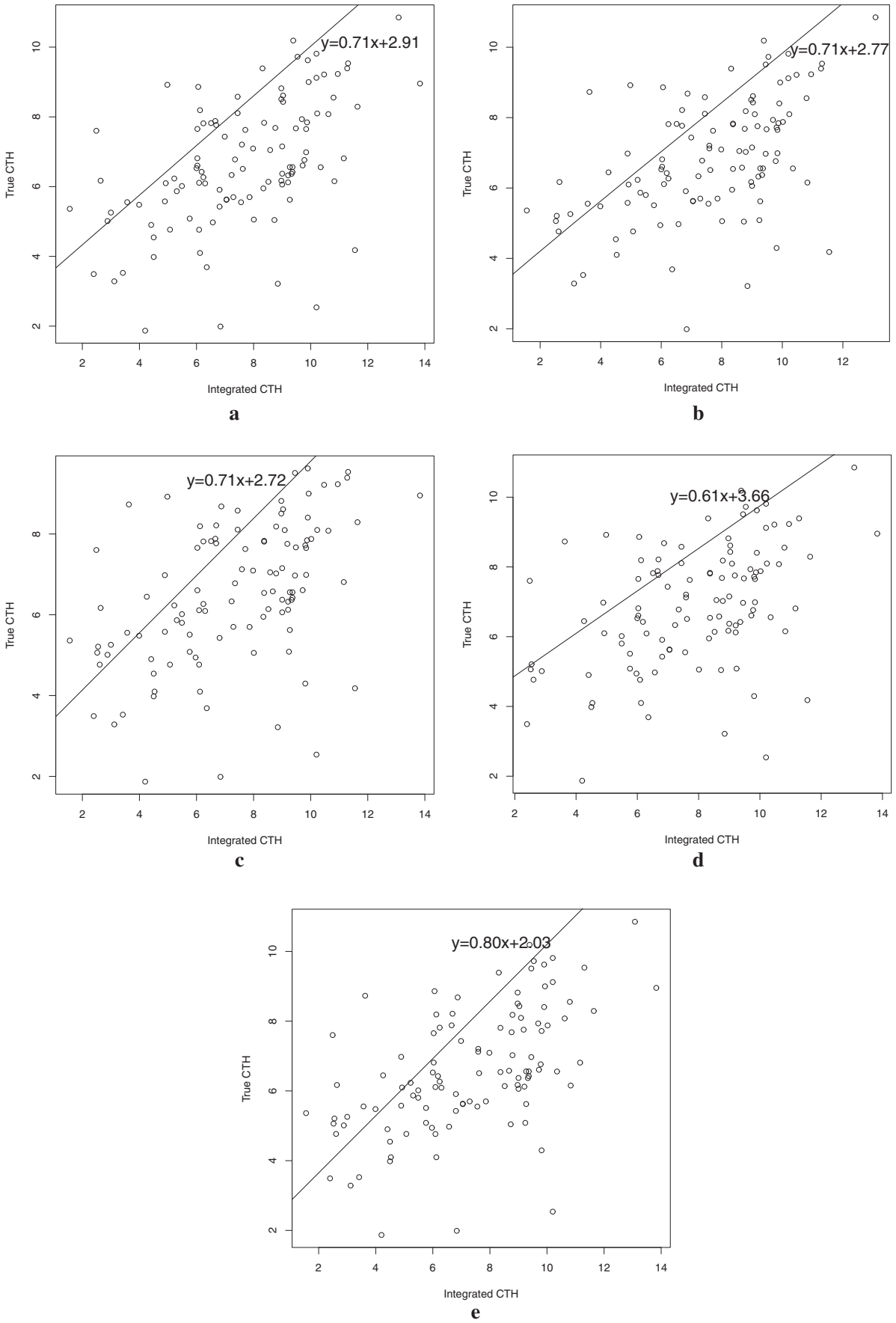

Fig. 3. The fitted lines with the "true" and integrated CTHs by Algorithm 1 corresponding to five folds in 5-fold cross validation.

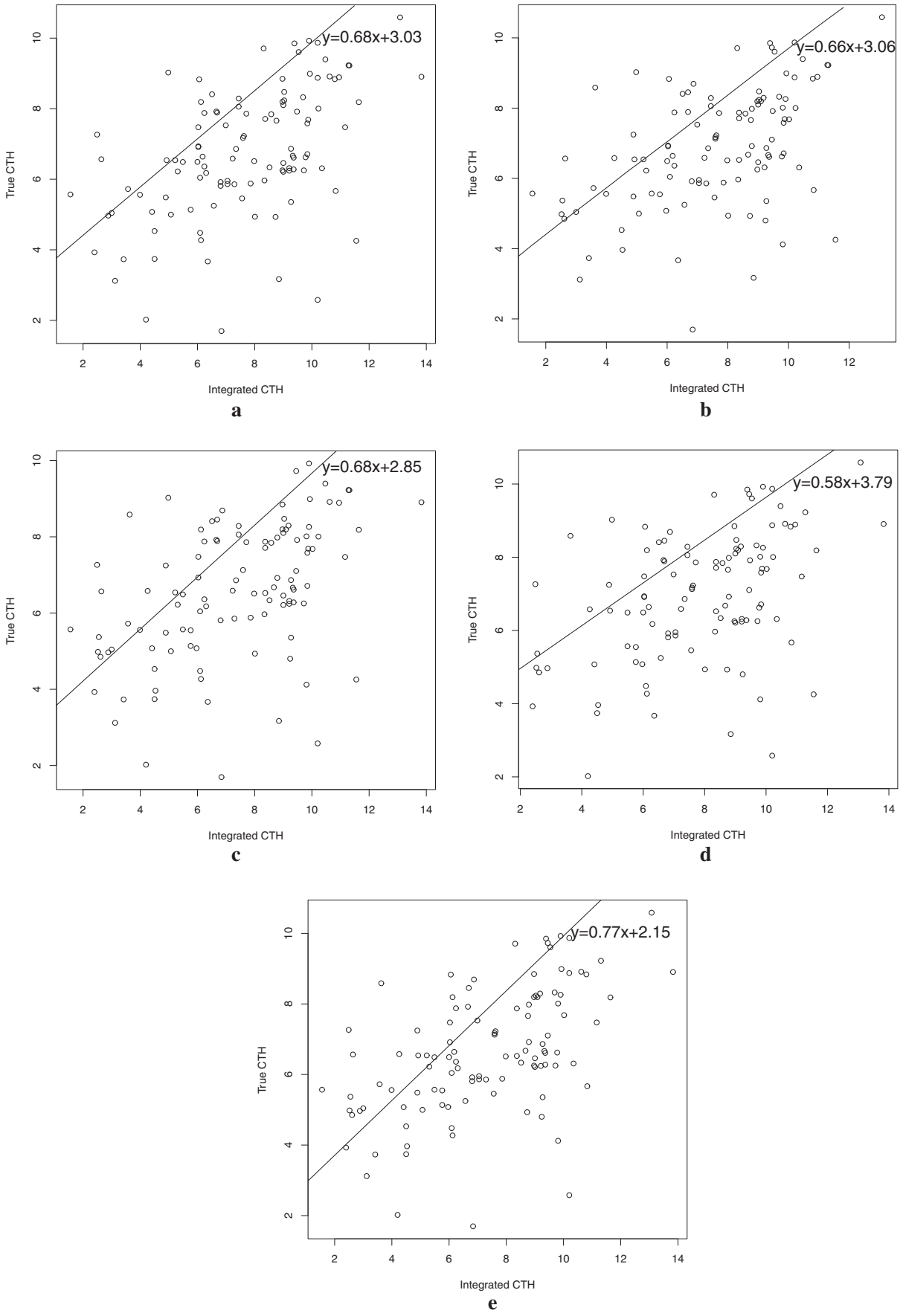

Fig. 4. The fitted lines with the "true" and integrated CTHs by Algorithm 2 corresponding to five folds in 5-fold cross validation.

Table 3
The results of correlation coefficient (Cor), mean square error (MSE), and bias (Bias) for different CTH observations.

CTH observation	Cor	MSE	Bias
Satellite	0.41	5.14	1.80
Radiosonde	0.20	5.95	2.03
Radar	0.42	5.11	1.78
Integration 1	**0.46**	**4.87**	**1.74**
Integration 2	0.44	4.99	1.77

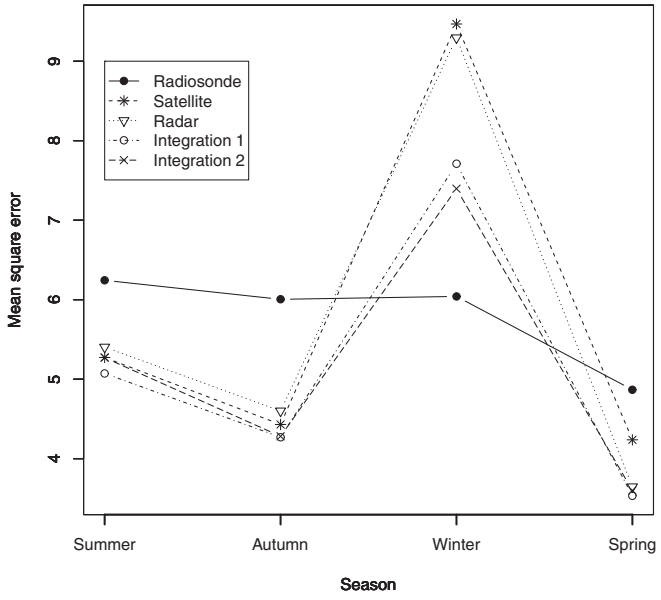

Fig. 5. The change of MSE for different seasons.

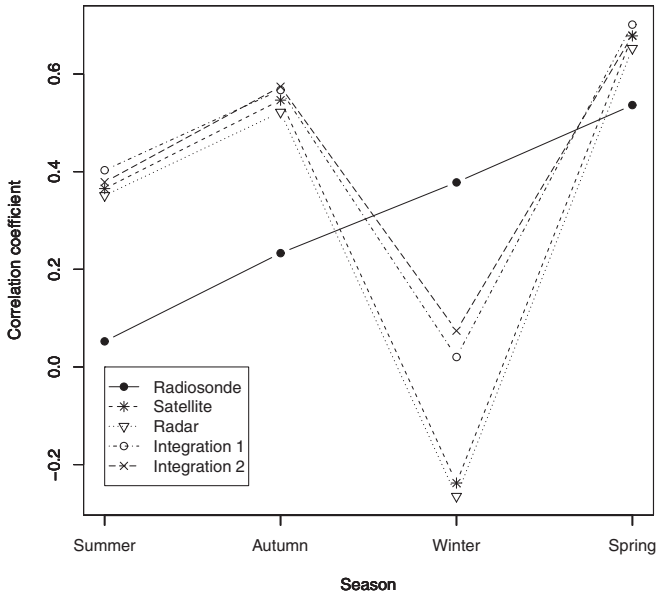

Fig. 6. The change of correlation coefficient for different seasons.

Acknowledgments

We thank the CMA Atmosphere Observation Test Bed and the National Satellite Meteorological Center of the CMA for providing the observational data support. We thank Zhe Wang and Fa Tao for the sharing and discussion of some data. This work was supported in part by the National Natural Science Foundation of China (NSFC) under Grant Nos. 61531019, 61601462, 61503228, and 71621002. and the Natural Science Foundation of Shanxi Province, China under Grant Nos. 201601D011046.

References

Bennett, A.F., 2002. Inverse Modeling of the Ocean and Atmosphere. Cambridge University Press.
Costa-Surós, M., Calbó-Angrill, J., González-Gutiérrez, J.A., Long, C.N., 2014. Comparing the cloud vertical structure derived from several methods based on measured atmospheric profiles and active surface measurements. Atmos. Measur. Tech. 7 (4), 2757–2773.
Dev, S., Wen, B., Lee, Y.H., Winkler, S., 2016. Machine learning techniques and applications for ground-based image analysis. IEEE Geosci. Remote Sen. Magaz. 4 (2), 79–93.
Dev, S., Lee, Y.H., Winkler, S., 2017. Color-based segmentation of sky/cloud images from ground-based cameras. IEEE J. Select. Topics Appl. Earth Observ. Remote Sens. 10 (1), 231–242.
Dybbroe, A., Karlsson, K., Thoss, A., 2005. Nwcsaf avhrr cloud detection and analysis using dynamic thresholds and radiative transfer modeling. part ii: tuning and validation. J. Appl. Meteorol. 44 (1), 55–71.
Garrett, T.J., Zhao, C., 2013. Ground-based remote sensing of thin clouds in the arctic. Atmos. Measur. Tech. 6 (5), 1227–1243.
Genkova, I., Seiz, G., Zuidema, P., Zhao, G., Girolamo, L.D., 2007. Cloud top height comparisons from aster, misr, and modis for trade wind cumuli. Remote Sens. Environ. 107 (1), 211–222.
Hastie, T., Tibshirani, R., Friedman, J., 2009. The Element of Statistical Learning. Springer.
Heinle, A., Macke, A., Srivastav, A., 2010. Automatic cloud classification of whole sky images. Atmos. Measur. Tech. 3 (3), 557–567.
Hirsch, E., Agassi, E., Koren, I., 2011. A novel technique for extracting clouds base height using ground based imaging. Atmos. Measur. Tech. 4 (1), 117–130.
Hollars, S., Fu, Q., Comstock, J., Ackerman, T., 2004. Comparisons of cloud-top height retrievals from ground-based 35 ghz mmcr and gms-5 satellite observations at arm twp manus site. Atmos. Res. 72 (1), 169–186.
Kalnay, E., 2003. Atmospheric Modeling, Data Assimilation, and Predictability. Cambridge University Press.
Lv, D., Wang, P., Qiu, J., Tao, S., 2003. An overview on the research progress of atmospheric remote sensing and satellite meteorology in China. J. Atmos. Sci. 27 (4), 552–566.
Marchand, R., Ackerman, T., Smyth, M., Rossow, W.B., 2010. A review of cloud top height and optical depth histograms from misr, isccp, and modis. J. Geophys. Res. Atmos. 115 (D16), 751–763.
Martucci, G., O'Dowd, C.D., 2011. Ground-based retrieval of continental and marine warm cloud microphysics. Atmos. Measur. Tech. 4 (4), 2749–2765.
Merino, A., Gascón, E., Del Peral, L., Reyes, M., Sáezcano, G., Rodriguez Frias, M., Soriano, J.F., Licandro, J., Hermida, L., Garcíaortega, E., 2016. Cloud top height estimation from wrf model: Application to the infrared camera onboard euso-balloon (cnes). In: Proceedings of the 34th ICRC, pp. 377.
Naud, C.M., Muller, J.P., Clothiaux, E.E., 2003. Comparison between active sensor and radiosonde cloud boundaries over the arm southern great plains site. J. Geophys. Res. Atmos. 108 (D4), 291–302.
Oh, S.B., Kim, Y.H., Kim, K.H., Cho, C.H., Lim, E., 2016. Verification and correction of cloud base and top height retrievals from kacband cloud radar in boseong, Korea. Adv. Atmos. Sci. 33 (1), 73–84.
Ricciardelli, E., Romano, F., Cuomo, V., 2008. Physical and statistical approaches for cloud identification using meteosat second generation-spinning enhanced visible and infrared imager data. Remote Sens. Environ. 112 (6), 2741–2760.
Stephens, G., 2005. Review article-cloud feedbacks in the climate system: a critical review. J. Clim. 18, 237–273.
Talagrand, O., 1997. Assimilation of observations, an introduction. J. Meteorol. Soc. Jpn. 75 (1), 191–209.
Viúdez-Mora, A., Costa-Surós, M., Calbó, J., González, J.A., 2015. Modeling atmospheric longwave radiation at the surface during overcast skies: the role of cloud base height. J. Geophys. Res. Atmos. 120 (1), 199–214.
Wang, J., Rossow, W.B., 1995. Determination of cloud vertical structure from upper-air observations. J. Appl. Meteorol. 34 (10), 2243–2258.
Wang, J., Rossow, W.B., Uttal, T., Rozendaal, M., 1999. Variability of cloud vertical structure during astex observed from a combination of rawinsonde, radar, ceilometer,

and satellite. Mon. Weather Rev. 127 (10), 2484.
Wang, Z., Wang, Z., Cao, X., Tao, F., 2018a. Comparison of cloud top heights derived from fy-2 meteorological satellites with heights derived from ground-based millimeter wavelength cloud radar. Atmos. Res. 199 (1), 113–127.
Wang, Y., Shi, C., Wang, C., Xiao, B., 2018b. Ground-based cloud classification by learning stable local binary patterns. Atmos. Res. 207 (7), 74–89.
Weisz, E., Li, J., Menzel, W.P., Heidinger, A.K., Kahn, B.H., Liu, C.Y., 2007. Comparison of airs, modis, cloudsat and calipso cloud top height retrievals. Geophys. Res. Lett. 34 (17), 251–270.
Wikle, C.K., Berliner, L.M., 2007. A bayesian tutorial for data assimilation. Physica D Nonlinear Phenomena 230 (1), 1–16.
J. Zhang, H. Chen, Z. Li, X. Fan, L. Peng, Y. Yu, M. Cribb, Analysis of cloud layer structure in shouxian, china using rs92 radiosonde aided by 95 ghz cloud radar. J. Geophys. Res. 115 (D7)
Zhang, Y., Zhang, W., Daren, L., Yongheng, B.I., 2014. Cloud top heights measured by metop-a iasi instrument compared with ground-based cloud radar. Chin. J. Atmos. Sci. 38 (5), 874–884.